Research Square

Preprints are preliminary reports that have not undergone peer review.
They should not be considered conclusive, used to inform clinical practice,
or referenced by the media as validated information.

Direct observation of double-layered reaction intermediates at the atomic scale during methane pyrolysis

Hui Wang
wanghui2020@email.tjut.edu.cn
Tianjin University of Technology
Yong-Li Shen
Tianjin University of Technology
Shengnan Yue
Fuzhou University https://orcid.org/0009-0002-1697-1242
Shanshan Liu
Tianjin University of Technology
Lin Gu
Tianjin University
Wenjuan Yuan
Tianjin University of Technology
Chao Zhang
Tsinghua University
Yu Huang
University of California Los Angeles https://orcid.org/0000-0003-1793-0741
Xiangfeng Duan
University of California, Los Angeles https://orcid.org/0000-0002-4321-6288
Wei Xi
Tianjin University
Tong-Bu Lu
Tianjin University of Technology https://orcid.org/0000-0002-6087-4880

Article

Keywords:

Posted Date: March 5th, 2026

DOI: https://doi.org/10.21203/rs.3.rs-8658713/v1

License: This work is licensed under a Creative Commons Attribution 4.0 International License.
Read Full License

Additional Declarations: There is **NO** Competing Interest.

Abstract

Direct observation of reaction intermediates at atomic scale is the most desired way to understand reaction mechanism. However, these transient intermediates during catalytic processes have never been directly observed thus far. Herein, we use in situ electron microscopy with high spatio-temporal resolution to directly probe reaction intermediates during methane pyrolysis over nanoporous Au. A double-layered reaction intermediate was discovered, comprising a chemisorbed –CH2 inner layer on the Au catalytic sites with a physisorbed CH4 outer layer, combined with electron energy-loss spectroscopy and in situ infrared spectroscopy. This structure was also confirmed by density functional theory calculations and Ab initio molecular dynamics. Further, we propose a CH4 substitution mechanism for the double-layered intermediates, wherein the physisorbed outer CH4 directly replenishes the chemisorbed inner –CH2 upon its consumption, while gaseous CH4 physisorbs on –CH2/Au to rebuild the double-layered intermediate structure. This provides unprecedented insights unraveling the molecular pathway of heterogeneous catalytic processes.

Introduction

Probing the reaction intermediates and molecular transformation pathway is central to understanding heterogeneous catalytic reaction mechanisms and designing new catalysts with tailored catalytic performance and selectivity[1–3]. To date, the identification of reaction intermediates generally relies on some indirect technologies, such as *in situ* infrared or Raman spectroscopy[4–6], leaving the specific adsorption sites and the exact morphological states of the reaction intermediates elusive and poorly resolved. The direct observation of transient reaction intermediates and atomic-scale structure dynamics could not only compensate for this limitation but also provide the most compelling evidence for elucidating the reaction pathways[7,8], yet represents a long-standing challenge.

The advancement of electron microscopy technology, especially the *in situ* technology, has opened the opportunity to directly observe the catalysts evolution and molecules adsorption on the catalyst surface, such as the directional migration and rapid coalescence of Au nanoparticles[9], the static adsorption of linear alkane and CO molecules on the surface of Au or Cu_xO[10–12], even the metastable oxygen species[13]. Additionally, *in situ* transmission electron microscopy (TEM) has been employed to probe the dynamic adsorption of H_2O molecules on the TiO_2 periodic surface during the water–gas shift reaction[14]. However, directly observing a transient intermediate and tracking its reaction pathway during the reaction remains a formidable challenge that has yet to be successfully demonstrated in experimental practice.

Herein, we employ *in situ* TEM with high spatial and temporal resolutions to directly probe the transient structure of the reaction intermediates of methane (CH_4) pyrolysis on nanoporous gold (NPG) catalysts. Methane pyrolysis is an attractive way to produce hydrogen (H_2) for the hydrogen economy[15–18]. NPG features rich periodic surfaces that facilitate molecular adsorption along specific directions, and can

catalyze CH_4 pyrolysis at a moderate temperature of ~350 °C[19]. More importantly, its freestanding negates the need for additional supports that could reduce contrast for adsorbed species by TEM[14]. Notably, our study for the first time reveals a dynamic intermediate with a double-layered structure, featuring a chemisorbed $–CH_2$ inner layer on the Au surface with a physisorbed CH_4 outer layer. Further, a CH_4 substitution mechanism for the double-layered reaction intermediates was proposed, in which the physisorbed CH_4 substitutes the chemisorbed carbon species to become the new chemisorbed inner layer, based on the *in situ* TEM observation and other characterizations.

Results

The double-layered adsorption structure. An NPG catalyst with the average ligament width of 30 nm (Fig. 1a) was prepared by a dealloying method[19–24]. The accelerating voltage of aberration-corrected TEM was optimized to achieve clearer imaging results (Supplementary Fig. 1). These TEM images demonstrate that the resulting NPG features zigzag surface structure (Supplementary Fig. 2a) with periodic atomic arrangement (Supplementary Fig. 2b–d). The lattice fringes of Au(111) plane were clearly observed in the high-resolution TEM image (Fig. 1b). Under vacuum and at 350 °C, the outermost layer spacing of 0.236 nm is identical to that of the inner layer. By contrast, the *in situ* observations performed at 350 °C during CH_4 pyrolysis revealed a typical expansion of the outermost layer spacing to 0.275 nm (Supplementary Fig. 3), with H_2 and carbon generation[19]. We note similar expansion of Au surface layer spacing was also observed upon CO adsorption[11], indicating the expansion may be induced by adsorbates.

The dynamic change of the surface layer spacing was further probed using time-resolved TEM studies upon exposure to CH_4 at high temperature (Fig. 1c). At 0.0000 s, the interlayer distances for both the outermost and inner layers were equal, with a measured value of 0.236 nm, at 350 °C in Ar. Surprisingly, the gradual expansion of the outermost layer spacing of Au atoms from the original value of 0.236 nm to 0.275 nm (i.e., an expansion of ~16%) was observed, after the ambient gas changed to CH_4 from Ar (9.3750 s). At 20.8750 s, the outermost interlayer spacing of Au atoms stabilized at 0.275 nm. This dynamic observation demonstrates that the expansion of the outermost layer of NPG is induced by the adsorbates generated during CH_4 pyrolysis.

Despite the observed expansion induced by adsorbates, resolving the formation process of adsorbates—particularly the critical transition from the invisible to visible states—is essential yet technically challenging for achieving atomic-scale morphological clarity[11,14]. For high-resolution observation of the adsorbed species, the zone axis of the target material must parallel to the direction of the electron beam when imaging. Further, an appreciable amount and a regular arrangement of these adsorbates are crucial[14]. After numerous attempts, the dynamic adsorption formation process was successfully captured at the initial stage of the reaction.

When NPG was exposed to a CH_4 atmosphere (Fig. 1d, Supplementary Video 1, 0.0000 s), the spacing of the outermost layer of Au(220) plane increased from 0.141 to 0.166 nm (by ~18%), indicating that certain adsorbates were present on the NPG surface. However, the adsorbates remained invisible due to the low contrast. At 0.1250 s, a quasi-regular array of tooth-shaped structures was observed for the adsorbates. Subsequently, the array became regular at 0.1625 s, with an average distance between neighboring “teeth” of 0.332 nm and a structure height of ~0.51 nm. The insets (0.1250 and 0.1625 s) reveal that the “teeth” are significantly larger than Au atoms, and appear to span between two Au atoms. It is noteworthy that these tooth-shaped structures are dynamically evolved over time (Supplementary Video 1).

In the other broader observation field, the tooth-shaped arrays became comb-shaped regular arrays (Fig. 2a and b), in which the comb teeth were longer and more uniform. Further, the spacing between neighboring comb teeth was 0.471 nm at the edge of Au(111) planes (Fig. 2a), whereas it was 0.433 nm at the edge of Au(220) planes (Fig. 2b). The interplanar spacings of the Au(111) and Au(220) planes are relatively large, providing sufficient space for multiple molecules to adsorb simultaneously with minimal mutual interference. Adjacent to the comb-shaped regular arrays, randomly arranged carbon products form amorphous carbon, whose morphology stands in sharp contrast to that of the regular array (Fig. 2a and b).

Notably, a double-layered structure with an interlayer spacing of 0.362 nm was observed at the edge of Au(111) planes, accompanied by a regular array structure in the vicinity with a comb-teeth spacing of 0.471 nm (Fig. 2c). Both structures exhibit identical heights, approximately 0.58 nm. Unexpectedly, a “crystalline structure” with well-resolved atom columns was observed (Fig. 2d), where each bright dot corresponds to an individual atom column. This contrast arises because all the atoms aligned parallel to the electron beam direction are projected as singular dots in transmission mode. The crystalline structure exhibited an approximate height of 0.58 nm, consistent with the double-layered structure and regular array (Fig. 2c and d). Additionally, the horizontal and vertical spacing between atom columns were 0.462 and 0.362 nm (Fig. 2d, inset), respectively, closely matching the structural characteristics of the double-layered structure and comb-shaped regular array. The similar structure height, interlayer and teeth spacings of adsorbates at the edge of same Au planes strongly suggest that these morphologically diverse features share identical adsorbates during CH_4 pyrolysis. The observed morphological variations may arise from distinct projection orientations relative to the TEM beam directions.

To confirm this inference, the evolution of the adsorption structures was monitored by *in situ* observation with high spatial and temporal resolutions. After extensive experimental trials, we successfully captured a specific configuration where the adsorbates’ zone axis perfectly paralleled to the direction of electron beam, and the adsorbates simultaneously aligned well along the projection direction (Fig. 3a, Supplementary Video 2). Evidently, a crystalline structure consisting of several discrete atom columns was observed at 0.0000 s (Fig. 3a, discrete magenta peaks were observed in the “Contrast” panels in Fig. 3b). However, the horizontal atom columns within a monolayer exhibited near-contiguous

alignment at 1.5250 s, forming a double-layered structure (Fig. 3c). They reverted to a discrete state at 1.8625 s. Additionally, the selected vertical adjacent atom columns were almost consecutive at 0.4375 s (Fig. 3d), and the entire morphology resembled comb teeth. Surprisingly, they reversed into the originally discrete state at 0.4500 s. The contrast was also confirmed by a simulation analysis (Supplementary Fig. 4). Similar evolution trend was also observed in another representative area (Supplementary Fig. 5). The above results conclusively demonstrate that these diverse adsorption morphologies originate from identical adsorbates, forming an essentially double-layered adsorption structure.

Identification as CH_4–CH_2/Au. The elucidation of the nature of the double-layered adsorbates has emerged as a paramount issue. First, neither the adsorbates nor the amorphous carbon is likely induced by the electron beam irradiation. Otherwise, only the irradiated regions can manifest such characteristics. However, we observed them throughout the entire sample region (Supplementary Fig. 6). Moreover, the *in situ* observation was performed in a flowing system (Supplementary Fig. 7), where all the introduced gases can be effectively purged to the ambient atmosphere. Before reaction, the samples were purged at 200 °C for 30 minutes with continuous Ar to remove the surface carbon deposition and residual air. Such pretreatments excluded the possibility of carbon contamination. Additionally, the adsorbates cannot be the previously reported AgO[24,25], as the interlayer and teeth spacings are entirely different from AgO, and no lattice fringes consistent with AgO has been detected. Given that the adsorbates were generated during the reaction, we infer they would be the reaction intermediates or products of CH_4 decomposition. The possible chemisorbed adsorbates may include CH_x, carbon products, or other carbon intermediates containing C–C or C=C bonds. Whereas the nonpolar and relatively stable CH_4 molecules are primarily physisorbed on the active sites[26,27].

To investigate the composition of the adsorbates, electron energy-loss spectroscopy (EELS) experiments were performed along a line from the background (supporting film) to NPG (Fig. 4a–c, Supplementary Figs. 8–10). At the point O—located closest to the NPG boundary yet still within the supporting film (Fig. 4a)—the image contrast exhibited a significant improvement over the background (Fig. 4b). Further, EELS analysis revealed two distinct spectral features in the carbon K-edge region (Fig. 4c): (i) a weak, broad peak at 293 eV corresponding to σ^* state absorption, indicating the presence of C–C single bond, and (ii) a minor shoulder at 285 eV attributed to π^* state absorption, corresponding to C=C double bonds[28,29]. Moving to point A, at 0.56 nm from O (Fig. 4a), the image contrast decreased modestly (Fig. 4b), while the intensity of carbon peaks at 285 eV enhanced slightly (Fig. 4c). At the more distant point B (Fig. 4a), a pronounced enhancement of carbon signals was observed despite the significant reduction in image contrast (Fig. 4b and c). The carbon signals exhibited progressive attenuation at point C (Fig. 4c), and almost disappeared at point D. Similar carbon signal tendency was consistently detected at other edge sites (Supplementary Figs. 8–10).

Given the long distance of OD (4.46 nm in Fig. 4a), the carbon signals of C–C and C=C species must originate from the amorphous carbon generated by CH_4 decomposition[19]. As the reaction proceeds rapidly under *in situ* TEM observation and carbon deposits form quickly, the clearly visible double-layered

adsorption structure exhibits only transient stability. In the case of the double-layered adsorbates in Fig. 3, the structure became obscured by amorphous carbon at 4.6750 s and was no longer visible at 17.2250 s (Supplementary Fig. 11). Thus, carbon signals of C–C and C=C species were inevitably detected by EELS.

Notably, the OA distance of ~0.56 nm approximates the height of double-layered adsorption structure at the edge of Au(111) planes (0.58 nm, Fig. 2c and d), while the other OA distances of ~0.49 nm (Supplementary Figs. 9 and 10) approaches the structure height for adsorption at the edge of Au(220) plane (0.51 nm, Fig. 1d). This suggests that the adsorbed species resides within the OA range. Interestingly, the carbon signals in OA are relatively weak despite the enhanced image contrast (Fig. 4a–c, and Supplementary Figs. 8–10). A reasonable explanation is that the adsorbates on NPG within the OA range lack the characteristic C–C or C=C bonds, i.e., CH_x. Otherwise, the presence of such carbon bonds would typically lead to enhanced spectral features rather than signal reduction. Consequently, these reaction intermediates shield the carbon signals to some extent. While the intermediates are continuously consumed and generated during the reaction, EELS can therefore detect the weak signals of amorphous carbon within the OA region. The shielding effect of reaction intermediates became less pronounced at NPG edges with fewer active sites and less carbon generation (Supplementary Figs. 12 and 13). Given the large heights (0.58 and 0.51 nm) and the presence of CH_x in the double-layered adsorption structure, we infer that it would be chemisorbed CH_x ($0 \le x \le 3$) followed by physisorbed CH_4 molecules.

To further verify the intermediate adsorbate species, *in situ* diffuse reflectance infrared Fourier-transform spectroscopy (DRIFTS) was performed under CH_4 pyrolysis conditions (Fig. 4d). The adsorption bands centered at 2915 and 2848 cm^{-1} were observed after the temperature was lowered from 350 °C. These two sets of vibrational modes are attributed to the asymmetric and symmetric stretching of $–CH_2$ species[4,30,31], respectively. This demonstrates that the primary chemisorbed species in the double-layered adsorption structure is $–CH_2$. Other possible species, such as C, –CH and $–CH_3$, are consumed or desorbed too rapidly to be detected, while the decomposition of $–CH_2$ to –CH would be the most challenging step. Unexpected, the CH_4 signal persisted after 30 minutes of Ar purging (Fig. 4e), whereas the vast majority of gaseous CH_4 had disappeared after just 5 minutes of purging. The residual CH_4 molecules would be the physisorbed species. With the combination of *in situ* TEM, EELS analysis and *in situ* DRIFTS, we can determine the double-layered structure to be CH_4–CH_2/Au, i.e., $–CH_2$ chemisorbed on NPG, and physisorbed CH_4 molecules stacked atop the $–CH_2$ species.

It is noteworthy that while TEM imaging revealed a more distinct double-layered adsorption structure at 350 °C (Supplementary Fig. 14), some localized regions retained this structure at 30 °C. The chemisorbed $–CH_2$ species can be detected more readily by DRIFTS below 350 °C, because most of the $–CH_2$ species are rapidly consumed and thereby barely detectable at 350 °C, whereas at lower

temperatures, the $-CH_2$ species are less mobile and reactive. This is analogous to the phenomenon where CH_4 molecules exhibit higher intensity at 30 °C than at 350 °C (Fig. 4d).

Theoretical analyses by DFT and AIMD. The double-layered reaction intermediate, CH_4–CH_2/Au, was comprehensively analyzed by density functional theory (DFT) calculations and *Ab initio* molecular dynamics (AIMD) (Fig. 5). When a CH_4 layer is stacked on top of the chemisorbed $-CH_2$ layer (Fig. 5a), the interlayer spacing of 0.360 nm and comb-teeth spacing of 0.475 nm (Fig. 5b) at the edge of Au(111) plane correspond well with the TEM observation (Fig. 5c). The intermediates adsorption configuration at the edge of Au(220) planes were also optimized in Supplementary Figs. 15 and 16. The sole inconsistency lies in the absence of the outermost layer expansion of Au atoms in the theoretical models. This difference arises because the outermost layer of actual NPG is discontinuous and lacks long-range order (Supplementary Fig. 17), whereas theoretical models preserve crystallographic integrity and periodicity.

Agreeing with the experimental results, the $-CH_2$ species chemisorbed on NPG with strong adsorption energies of ~3.6 eV (Supplementary Fig. 18). The long distance between $-CH_2$ and CH_4 (0.360 nm in Fig. 5 and 0.246 nm in Supplementary Fig. 15) has already exceeded the typical range of chemical bonds. Further, the adsorption of outer CH_4 on the inner $-CH_2$ was weak with energies ranging from −0.10 to −0.19 eV (Supplementary Fig. 18). This weak adsorption is similar to CH_4 physisorbed on NPG, with energies ranging from −0.19 to −0.21 eV (Supplementary Fig. 19). We next performed partial density of states analysis by DFT (Fig. 5d) to investigate the electron distribution of $-CH_2$, CH_4 and Au atoms. It was found that there is an overlapping between the d band of top-layer Au and the p band of C in $-CH_2$, but hardly overlap between Au atoms and CH_4 molecules in the second layer. This demonstrates that a chemical bond forms between $-CH_2$ and the surface Au atoms, whereas the outer CH_4 molecules exhibit almost no interaction with the surface Au atoms.

To further clarify the interactions between $-CH_2$ and CH_4, CH_4 and Au planes in the double-layered structure, an independent gradient model (IGM) analysis was performed[32,33], in which the adsorbed $-CH_2$ and isolated CH_4 molecule are defined as two independent fragments (Supplementary Fig. 20 and Fig. 5e). The scatter diagram of the δ_g descriptors versus the signed electron density (sign(λ_2)ρ) shows two independent $\delta_{g,inter}$ peaks at approximately −0.04 and 0.04 (Supplementary Fig. 20). The electron densities in these two regions were relatively small, but significantly higher than zero, which demonstrates the weak interaction between $-CH_2$ and CH_4. Both the magnified view of $\delta_{g,inter}$ (Fig. 5e) and isosurface of $\delta_{g,inter}$ (inset, Fig. 5e) confirmed that a van der Waals interaction exists between $-CH_2$ and CH_4, i.e., physisorption. The little interaction between CH_4 and Au(111) surface in the double-layered adsorption structure was also verified by the IGM method (Supplementary Fig. 21). Similar analyses in other adsorption circumstances further confirmed the physical interactions between $-CH_2$ and CH_4 (Supplementary Figs. 22, 23).

More so, we performed AIMD to evaluate whether CH_4 can adsorb on the active $–CH_2$/Au ensemble. The energy of the double-layered adsorption structure behaves quite stable during the AIMD simulation running for 2 ps (Fig. 5f), indicating this adsorption structure is practically reasonable. For the dynamic structure (Supplementary Video 3), the CH_4 molecules can adsorb on $–CH_2$/Au to form a stable layer and maintain for a period during the reaction. Beyond that, the entire adsorption structures exhibited persistent oscillatory motions. This strongly supports that the TEM-observed double-layered adsorption structure is metastable and transient, rather than stable and changeless. Hence, the TEM-observed double-layered structure is rationally attributed to CH_4–CH_2/Au.

Proposed CH_4 substitution mechanism. Generally, physisorption is ubiquitous in many reactions, yet its role remains unclear. Most reports focus exclusively on chemisorption, as it demonstrably contributes to the reaction, while physisorption is often overlooked. The double-layered adsorption structure observed in this study suggests that, although the noncovalent interaction between $–CH_2$ and CH_4 is relatively weak, it is capable of dissipating the energy of CH_4 molecules (mostly translational and rotational) to reach an adsorption equilibrium with the underlying $–CH_2$. Therefore, physisorption in the double-layered adsorption structure facilitates the capture of gaseous CH_4 reactant molecules.

Further, DFT calculations based on *in situ* observations were conducted to investigate the possible influence of physisorption on CH_4 pyrolysis pathway. Surprisingly, the Au surface is not static, but exhibits dynamic wave-like undulations (Supplementary Video 4) with the reaction intermediates and products adsorbing on the surface. Given the intricate surface dynamics, the most frequently exposed Au(111) plane[34] was selected for further DFT calculations. The calculated activation energy for $–CH_2$ decomposition decreased owing to the physisorption of CH_4 molecules (Fig. 6a–c), compared with the exclusive adsorption of $–CH_2$ species. Therefore, chemisorbed $–CH_2$ captures gaseous CH_4 by physisorption, whereas physisorbed CH_4 facilitates the decomposition of $–CH_2$ in the double-layered structure. Due to the dynamic nature of the actual NPG active sites during the reaction, DFT calculations can only substantiate up to this stage.

To explore the reaction pathway of the double-layered intermediates, more *in situ* observations were performed (Fig. 6d and Supplementary Video 5). At 0.0000 s, the height of the teeth-shaped intermediates (indicated by the arrow) was approximately 0.51 nm, it decreased to ~0.27 nm at 0.0625 s, and restored to its original height at 0.1875 s. This indicates that, once the chemisorbed $–CH_2$ was consumed, it would be rapidly replenished by physisorbed CH_4 closely stacked at the outer layer, forming new chemisorbed $–CH_2$ species. Meanwhile, new gaseous CH_4 molecules physisorb on $–CH_2$ species to rebuild the double-layered CH_4–CH_2/Au structure. At 0.4500 s, the adsorption intermediate indicated by the arrow was almost invisible. For this moment, most of the $–CH_2$ may have just reacted to C atoms to remove, and the outer physisorbed CH_4 was in the process of substituting it, causing neither the inner nor outer species aligns to a straight line. At 0.5125 s, the structure height became 0.19 nm, indicating the chemisorbed $–CH_2$ aligned in the electron beam

direction. Notably, this height was shorter than that at 0.0625 s (0.27 nm). This discrepancy may arise from the two distinct transient states during the replenishment of physisorbed CH_4 for chemisorbed $–CH_2$. At 0.7250 s, the whole structure height of 0.51 nm appeared again, indicating the restoration of the double-layered intermediates.

Further, when temperature programmed desorption (TPD) was performed on the reaction-spent NPG from Fig. 4e—which had been subjected to a 30-minute Ar purge yet retained physisorbed CH_4—the analysis revealed no detectable CH_4 signal (Fig. 6e); only H_2 desorption was observed. This indicates that the physisorbed CH_4 underwent substitution to form chemisorbed $–CH_2$ species (Fig. 6f), ultimately transforming into carbon and H_2. Notably, the majority of H_2 signals in TPD originate from the residual fraction that failed to desorb during cooling to ambient temperature. The combination of *in situ* TEM observation and TPD demonstrated that the physisorbed CH_4 in the double-layered reaction intermediates acts as a substitute for the chemisorbed $–CH_2$ species.

The conventional *in situ* technologies for reaction intermediates can only demonstrate the existence of chemisorbed and physisorbed species during CH_4 pyrolysis. Nevertheless, the adsorption sites for these adsorbates remain unidentified, and it is unknown whether chemisorbed and physisorbed species occupy discrete surface sites. The direct observation of these reaction intermediates by *in situ* TEM with high spatio-temporal resolution provides detailed information on their existing states and position, we therefore discovered the double-layered physi-chemisorbed adsorption structure. Further, the combined *in situ* TEM and TPD analyses provide direct evidence for the CH_4 substitution mechanism within the double-layered reaction intermediates. This mechanism is rather different from the conventional, in which the active metal site directly captures a new adsorbate from the gaseous phase after the original adsorbate molecule is converted and desorbed. By contrast, the double-layered adsorption structure eliminates the traditional step involving the direct capture of atmospheric gas molecules by active metal sites to form new adsorbates. This mirrors an automatic “machine gun”, contrasting with the “bolt-action rifle” operation of the conventional mechanism.

Conclusions

In this study, CH_4 pyrolysis was selected as a probe reaction to study the intermediate structure formed during the reaction, which was firstly visualized to be double-layered adsorption comprising chemisorbed $–CH_2$ with physisorbed CH_4 stacked atop. Beyond this, we proposed a CH_4 substitution mechanism in the double-layered reaction intermediates: once the inner chemisorbed $–CH_2$ was consumed, the outer physisorbed CH_4 would substitute it to form new chemisorbed $–CH_2$ species. This renews the fundamental understanding of reaction mechanism in heterogeneous catalysis and brings novel perspectives for atomic-level reaction pathways.

Methods

NPG preparation. The NPG samples were synthesized by a dealloying method, as previously reported[19,22–24,35,36]. An Au–Ag alloy film with the thickness of 100 nm was firstly immersed in concentrated HNO_3 at 10 °C for 1 hour to remove the alloyed Ag. As we previously reported[19], the residual Ag accounted for 1.37 ± 0.38 at.%, and evenly distributed in NPG. The sample was rinsed with ultrapure water at least three times to remove the residual HNO_3, and the eventually obtained NPG samples could float on the surface of ultrapure water.

***In situ* electron microscopy experiments.** The conventional TEM, scanning transmission electron microscopy, and aberration-corrected objective TEM images were obtained from three different instruments of Talos F200X, Titan Cubed Themis G2 300, and Themis Z from Thermo Fisher Scientific at 200 kV, respectively. Pertaining to the *in situ* TEM experiments, the DENSsolutions chip was integrated with 9 observation windows fabricated from Si_3N_4 films, and the NPG sample was encapsulated between the upper and lower Si_3N_4 films with the total thickness of ~50 nm. This Si_3N_4 film window may introduce slight image blurring, but preserves the accuracy of atomic spacing measurements due to the parallel impact on image contrast of different regions. After the chip was loaded with tiny NPG pieces, we assembled it into the *in situ* gas-phase holder (Climate S3 +, DENSsolutions). Its temperature error is lower than 5%. The gas-phase holder was subsequently installed into Themis Z or Talos F200X recording the movies/images in real time with a high-speed camera of 80 frames per second (Ceta 2, Thermo Fisher Scientific). Both the Themis Z or Talos F200X were operated at 200 kV, and the dose rate of the electron beam applied for these *in situ* experiments was 0.039–1570 $eÅ^{-2}$ s^{-1}, which corresponds to the magnification of ×4300 to ×1,050,000. Before the *in situ* experiment, all gas pipes and the chip were flushed with Ar at 200 °C for 30 minutes at 0.1 MPa to remove the surface carbon deposition and the residual air in the system. Afterwards, pure CH_4 was introduced to the gas-phase holder instantly. Subsequently, the sample was heated to 350 °C at a rate of 30 °C/min, and the reaction intermediate structures and movies were recorded at that temperature. The CH_4 and Ar gases with high purity were purchased from Beijing ZG Special Gases Science & Technology Co., Ltd (Beijing, China).

***In situ* DRIFTS under CH_4 pyrolysis conditions and TPD.** The *in situ* DRIFTS under CH_4 pyrolysis conditions were collected on a Nicolet 6700 FTIR equipped with a PIKE sample cell and an MCT detector at the resolution of 4 cm^{-1}. In the implementation of *in situ* DRIFTS experiment, the sample cell was first ramped to 350 °C from room temperature in Ar, and held at that temperature for about 30 minutes. The background spectra were collected during the holding time at 350 °C after the temperature and circumstance stabilized. Afterwards, Ar was stopped, CH_4 was flowed into the sample cell for about 30 minutes, and the evolution of sample spectra was recorded every 10 seconds. Subsequently, the sample cell was cooled down to room temperature with continuous spectral monitoring, during which the CH_4 supply was systematically terminated. To investigate whether the physisorbed CH_4 would desorb, we subsequently performed a Ar purge on the above reaction-spent NPG with continuous spectral monitoring. Specifically, pure Ar was introduced to the chamber at a flow rate of 50 mL/min, which was supposed to remove all gaseous CH_4 within several minutes. After that, CH_4 TPD was conducted on a

ChemStar Quantachrome equipment combined with mass spectroscopy (MS) to analyze the trace CH_4 and H_2. Typically, ~50 mg of the reaction-spent NPG that was subjected to 30 minutes of Ar purging, was ramped to 500 °C at 10 °C/min in He purge with the flow rate of 50 mL/min, meanwhile recording the MS signal.

Computational methodology. All the structure optimizations presented in this work were conducted by Vienna ab initio Simulation Package (VASP) code[37,38]. The ionic cores were described by the projector augmented wave (PAW) method[39]. The exchange-correlation functional was described using the generalized gradient approximation (GGA)-Perdew, Burke, and Ernzerhof (PBE) functional.[40] The energy cutoff was set to be 450 eV. The double-layered structures on NPG observed from <011>, <111> and <001> were established by a CH_4 molecule stacked atop $-CH_2$ species which adsorbed on (3-11), (0-11) and (012) surface ((1×1) unit cell) with coverage equal to 0.5 ML. The coverage was set to be 0.5 ML to avoid any interactions between the neighboring adsorbed species. NPG catalysts of these double-layered configurations are composed of six ((3-11) and (0-11)) or eight ((012)) Au layers. The $-CH_2$ decomposition process was calculated using a (4×4) and five-layer Au(111) model. In all calculations, the bottom two Au layers were fixed at their bulk positions, while others, as well as adsorbates, were allowed to relax during the calculations. The transition states (TS) calculations for $-CH_2$ decomposition with and without CH_4 adsorption were carried out through a two-step approach. First, a series of structures along the reaction path have been calculated using the climbing nudged elastic band (CI-NEB) method. Afterwards, the configuration with the highest energy was chosen as input for dimer calculation to optimize the TS structure[41]. The optimization thresholds for structure optimization, CI-NEB, and dimer calculation were set to be 10^{-5} eV and 0.02 eV $Å^{-1}$ for electronic and ionic relaxations, respectively. Noteworthy, the van der Waals corrections by applying Grimme's DFT-D3 method was included in all the above calculations[42]. The Brillouin zone was sampled by a Gamma-centered k-point mesh generated through the Monkhorst–Pack method[43], and all KPOINTS files for SCF calculation were generated using VASPKIT Program[44], the accuracy level was set to medium (0.04) in VASPKIT, and (5 × 7 × 1) for (012), (6 × 4 × 1) for (0-11), (5 × 5 × 1) for (3-11). The independent gradient model (IGM) analysis for the interaction between CH_4 and $-CH_2$ was carried out by Multiwfn[45]. The adsorption energy was calculated by the formula below:

$$E_{ad} = E_{CH4}* - E* - E_{CH4}$$

where $E_{CH4}*$ is the energy of adsorbed CH_4; E* represents the energy of the catalyst; E_{CH4} is the energy of CH_4 molecule.

The AIMD for the double-layered structure was carried out by the CP2K package, based on PBE functional and a hybrid Gaussian/Plane-Wave scheme (GPW) [46]. The GTH pseudopotentials were chosen to describe the core electrons[47,48]. The wave functions were expanded in optimized double-ζ Gaussian basis sets[49], and the plane waves were expanded with a cutoff energy of 400 Rydberg. The

theoretical model for the double-layered structure was constructed based on our geometric structure optimization, i.e., CH_4–CH_2 double-layered adsorption structure on a four atom layers (2√2 × 3)R30° Au(111) surface, and the vacuum space was set to be 15 Å to avoid the interaction between two neighboring structures. The Γ-point approximation was employed for Brillouin Zone integration. Meanwhile, the convergence threshold of density matrix of inner SCF was set to be 1×10^{-5}. During the calculation, the bottom two Au layers were fixed in their bulk positions, and the other layers and the adsorbates were all allowed to relax. The input file for calculation was generated using Multiwfn[45,50].

Declarations

Data Availability

All data supporting the findings of this study are available within the Article and its Supplementary Information. Additional data are available from the corresponding authors upon reasonable request.

Acknowledgements

This work was financially supported by the National Key R&D Program of China (2017YFA0700104), the National Natural Science Foundation of China (21931007, 22301215, 22531007), and Chunhui Program from the Ministry of Education (HZKY20220602). We acknowledge the National Supercomputing Center in Shenzhen for providing computational resources and VASP software. We thank Prof. Meiqing Shen at Tianjin University for providing the infrared instruments to perform DRIFTS experiments, and Xun Wang at Tsinghua University for elucidating the CH_4 pyrolysis pathway.

Author contributions

H. W. processed most of the electron microscopy images and videos under the guidance of W. X., performed the DRIFTS experiments and drafted the experimental section of the manuscript. Y. S. conducted the theoretical calculations and drafted the corresponding part of the manuscript. S. Y., S. L., L. G., and W. Y., facilitated the TEM observations. C. Z. contributed to sample and manuscript preparation. W. X. conducted the *in situ* TEM observations during the CH_4 pyrolysis reaction. Y. H. and X. D. discussed and revised the manuscript. W. X. and T. L. conceptualized the research study, supervised, and led the project.

Competing interests

The authors declare no competing financial interests.

Additional information

Additional materials are available for this paper at https://doi.org/

Correspondence and requests for materials should be addressed to T-B. L., W. X and H. W.

References

1. Espenson, J. H. *Chemical Kinetics and Reaction Mechanisms*. (McGraw-Hill, Inc., 1995).
2. Masel, R. I. *Principles of Adsorption and Reaction on Solid Surfaces*. (John Willey & Sons, 1996).
3. Guo, X. *et al.* Direct, nonoxidative conversion of methane to ethylene, aromatics, and hydrogen. *Science* **344**, 616–619 (2014).
4. *Infrared Spectroscopy: Fundamentals and Applications*. (John Wiley & Sons, Ltd, Chichester, UK, 2005).
5. Chabal, Y. J. Surface infrared spectroscopy. *Surf. Sci. Rep.* **8**, 211–357 (1988).
6. Wang, H. *et al.* Surface reactive oxygen from support corrects the nominal supported metal size effect in controlling the reactivity for low-temperature CH_4/CO_2 reforming. *ACS Catal.* **14**, 10712–10727 (2024).
7. Wang, R. The dynamics of the peel. *Nat. Catal.* **3**, 333–334 (2020).
8. Zhao, H. *et al.* Atomic-scale structure dynamics of nanocrystals revealed by *in situ* and environmental transmission electron microscopy. *Adv. Mater.* **35**, 2206911 (2023).
9. Cao, Y. *et al.* Directional migration and rapid coalescence of Au nanoparticles on anisotropic ReS_2. *Nano Lett.* **23**, 1211–1218 (2023).
10. Zhong, D. *et al.* Linear alkane polymerization on a gold surface. *Science* **334**, 213–216 (2011).
11. Yoshida, H. *et al.* Visualizing gas molecules interacting with supported nanoparticulate catalysts at reaction conditions. *Science* **335**, 317–319 (2012).
12. Hensley, A. J. R. *et al.* CO adsorption on the “29” $Cu_xO/Cu(111)$ surface: An integrated DFT, STM, and TPD study. *J. Phys. Chem. C* **120**, 25387–25394 (2016).
13. Sandoval-Diaz, L. *et al.* Metastable nickel–oxygen species modulate rate oscillations during dry reforming of methane. *Nat. Catal.* **7**, 161–171 (2024).
14. Yuan, W. *et al.* Visualizing H_2O molecules reacting at TiO_2 active sites with transmission electron microscopy. *Science* **367**, 428–430 (2020).
15. Ashik, U. P. M., Wan Daud, W. M. A. & Abbas, H. F. Production of greenhouse gas free hydrogen by thermocatalytic decomposition of methane – A review. *Renewable Sustainable Energy Rev.* **44**, 221–256 (2015).
16. Nikolaidis, P. & Poullikkas, A. A comparative overview of hydrogen production processes. *Renewable Sustainable Energy Rev.* **67**, 597–611 (2017).
17. Upham, D. C. *et al.* Catalytic molten metals for the direct conversion of methane to hydrogen and separable carbon. *Science* **358**, 917–921 (2017).
18. Palmer, C. *et al.* Methane pyrolysis with a molten Cu–Bi alloy catalyst. *ACS Catal.* **9**, 8337–8345 (2019).

19. Xi, W. *et al.* Dynamic co-catalysis of Au single atoms and nanoporous Au for methane pyrolysis. *Nat. Commun.* **11**, 1919 (2020).
20. Wittstock, A., Zielasek, V., Biener, J., Friend, C. M. & Baumer, M. Nanoporous gold catalysts for selective gas-phase oxidative coupling of methanol at low temperature. *Science* **327**, 319–322 (2010).
21. Sun, S., Chen, X., Badwe, N. & Sieradzki, K. Potential-dependent dynamic fracture of nanoporous gold. *Nat. Mater.* **14**, 894–898 (2015).
22. Fujita, T. *et al.* Atomic origins of the high catalytic activity of nanoporous gold. *Nat. Mater.* **11**, 775–780 (2012).
23. Liu, P. *et al.* Visualizing under-coordinated surface atoms on 3D nanoporous gold catalysts. *Adv. Mater.* **28**, 1753–1759 (2016).
24. Kamiuchi, N. *et al.* Self-activated surface dynamics in gold catalysts under reaction environments. *Nat. Commun.* **9**, 2060 (2018).
25. Zugic, B. *et al.* Dynamic restructuring drives catalytic activity on nanoporous gold–silver alloy catalysts. *Nat. Mater.* **16**, 558–564 (2017).
26. Schwach, P., Pan, X. & Bao, X. Direct conversion of methane to value-added chemicals over heterogeneous catalysts: Challenges and prospects. *Chem. Rev.* **117**, 8497–8520 (2017).
27. Thyssen, V. V., Vilela, V. B., de Florio, D. Z., Ferlauto, A. S. & Fonseca, F. C. Direct conversion of methane to C_2 hydrocarbons in solid-state membrane reactors at high temperatures. *Chem. Rev.* **122**, 3966–3995 (2022).
28. Martin, J. M., Vacher, B., Ponsonnet, L. & Dupuis, V. Chemical bond mapping of carbon by image-spectrum EELS in the second derivative mode. *Ultramicroscopy* **65**, 229–238 (1996).
29. Graphite and diamond C-K Edge Spectra | David Muller, Applied Physics Group @Cornell. https://muller.research.engineering.cornell.edu/spectra/graphite-and-diamond-c-k-edge-spectra/.
30. Bachiller-Baeza, B. *et al.* Transient studies of low-temperature dry reforming of methane over Ni-CaO/ZrO_2-La_2O_3. *Appl. Catal., B* **129**, 450–459 (2013).
31. Zhang, S., Li, Y., Knoll, A. & Oehrlein, G. S. Mechanistic aspects of plasma-enhanced catalytic methane decomposition by time-resolved operando diffuse reflectance infrared Fourier transform spectroscopy. *J. Phys. D: Appl. Phys.* **53**, 215201 (2020).
32. Lefebvre, C. *et al.* Accurately extracting the signature of intermolecular interactions present in the NCI plot of the reduced density gradient versus electron density. *Phys. Chem. Chem. Phys.* **19**, 17928–17936 (2017).
33. Lu, T. & Chen, Q. Independent gradient model based on Hirshfeld partition: A new method for visual study of interactions in chemical systems. *J. Comput. Chem.* **43**, 539–555 (2022).
34. Hou, X. *et al.* Complete surface reconstruction of nanoporous gold during CH_4 pyrolysis. *Nanoscale* **14**, 8023–8027 (2022).

35. Fujita, T. *et al.* Atomic observation of catalysis-induced nanopore coarsening of nanoporous gold. *Nano Lett.* **14**, 1172–1177 (2014).
36. Ding, Y., Kim, Y. -J. & Erlebacher, J. Nanoporous gold leaf: “Ancient technology”/Advanced material. *Adv. Mater.* **16**, 1897–1900 (2004).
37. Kresse, G. & Furthmüller, J. Efficient iterative schemes for *ab initio* total-energy calculations using a plane-wave basis set. *Phys. Rev. B* **54**, 11169–11186 (1996).
38. Kresse, G. & Furthmüller, J. Efficiency of ab-initio total energy calculations for metals and semiconductors using a plane-wave basis set. *Comput. Mater. Sci.* **6**, 15–50 (1996).
39. Blöchl, P. E. Projector augmented-wave method. *Phys. Rev. B* **50**, 17953–17979 (1994).
40. Perdew, J. P., Burke, K. & Ernzerhof, M. Generalized gradient approximation made simple. *Phys. Rev. Lett.* **77**, 3865–3868 (1996).
41. Ricciardulli, T. *et al.* Effect of Pd coordination and isolation on the catalytic reduction of O2 to H2O2 over PdAu bimetallic nanoparticles. *J. Am. Chem. Soc.* **143**, 5445–5464 (2021).
42. Grimme, S., Antony, J., Ehrlich, S. & Krieg, H. A consistent and accurate ab initio parametrization of density functional dispersion correction (DFT-D) for the 94 elements H-Pu. *J. Chem. Phys.* **132**, 154104 (2010).
43. Monkhorst, H. J. & Pack, J. D. Special points for Brillouin-zone integrations. *Phys. Rev. B* **13**, 5188–5192 (1976).
44. Wang, V., Xu, N., Liu, J.-C., Tang, G. & Geng, W.-T. VASPKIT: A user-friendly interface facilitating high-throughput computing and analysis using VASP code. *Comput. Phys. Commun.* **267**, 108033 (2021).
45. Lu, T. & Chen, F. Multiwfn: A multifunctional wavefunction analyzer. *J. Comput. Chem.* **33**, 580–592 (2012).
46. VandeVondele, J. *et al.* Quickstep: Fast and accurate density functional calculations using a mixed Gaussian and plane waves approach. *Comput. Phys. Commun.* **167**, 103–128 (2005).
47. Goedecker, S., Teter, M. & Hutter, J. Separable dual-space Gaussian pseudopotentials. *Phys. Rev. B* **54**, 1703–1710 (1996).
48. Hartwigsen, C., Goedecker, S. & Hutter, J. Relativistic separable dual-space Gaussian pseudopotentials from H to Rn. *Phys. Rev. B* **58**, 3641–3662 (1998).
49. VandeVondele, J. & Hutter, J. Gaussian basis sets for accurate calculations on molecular systems in gas and condensed phases. *J. Chem. Phys.* **127**, 114105 (2007).
50. Lu, T. A comprehensive electron wavefunction analysis toolbox for chemists, Multiwfn. *J. Chem. Phys.* **161**, 082503 (2024).

Figures

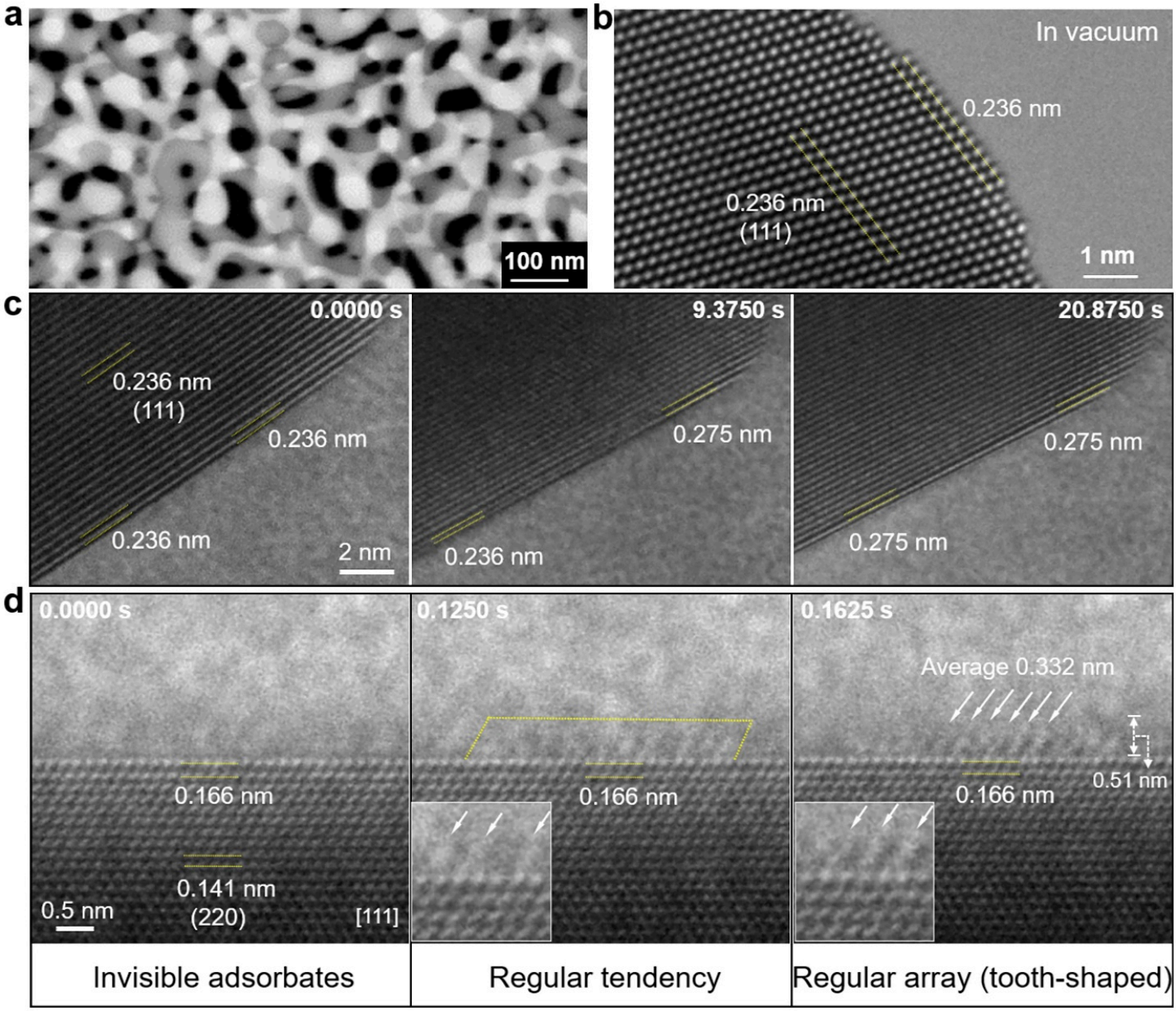


Figure 1

Surface structures analysis of NPG before and after CH_4 introduction. a, Scanning transmission electron microscopy image of NPG. **b,** TEM image of NPG under vacuum conditions at 350 °C. **c,** The expansion process of outermost layer spacing of Au(111) plane induced by adsorbates. The outermost layer spacing was expanded from 0.236 to 0.275 nm with the atmosphere switched from Ar to CH_4. **d,** The formation process of the adsorption structure at the edge of Au(220) plane. A quasi-regular pattern of adsorption structure was observed at 0.1250 s (yellow dashed box), and a tooth-shaped regular array formed at 0.1625 s, with an average tooth-spacing of 0.332 nm and a structure height of ~0.51 nm. The insets show an enlarged image of the adsorption structure at the corresponding moment.

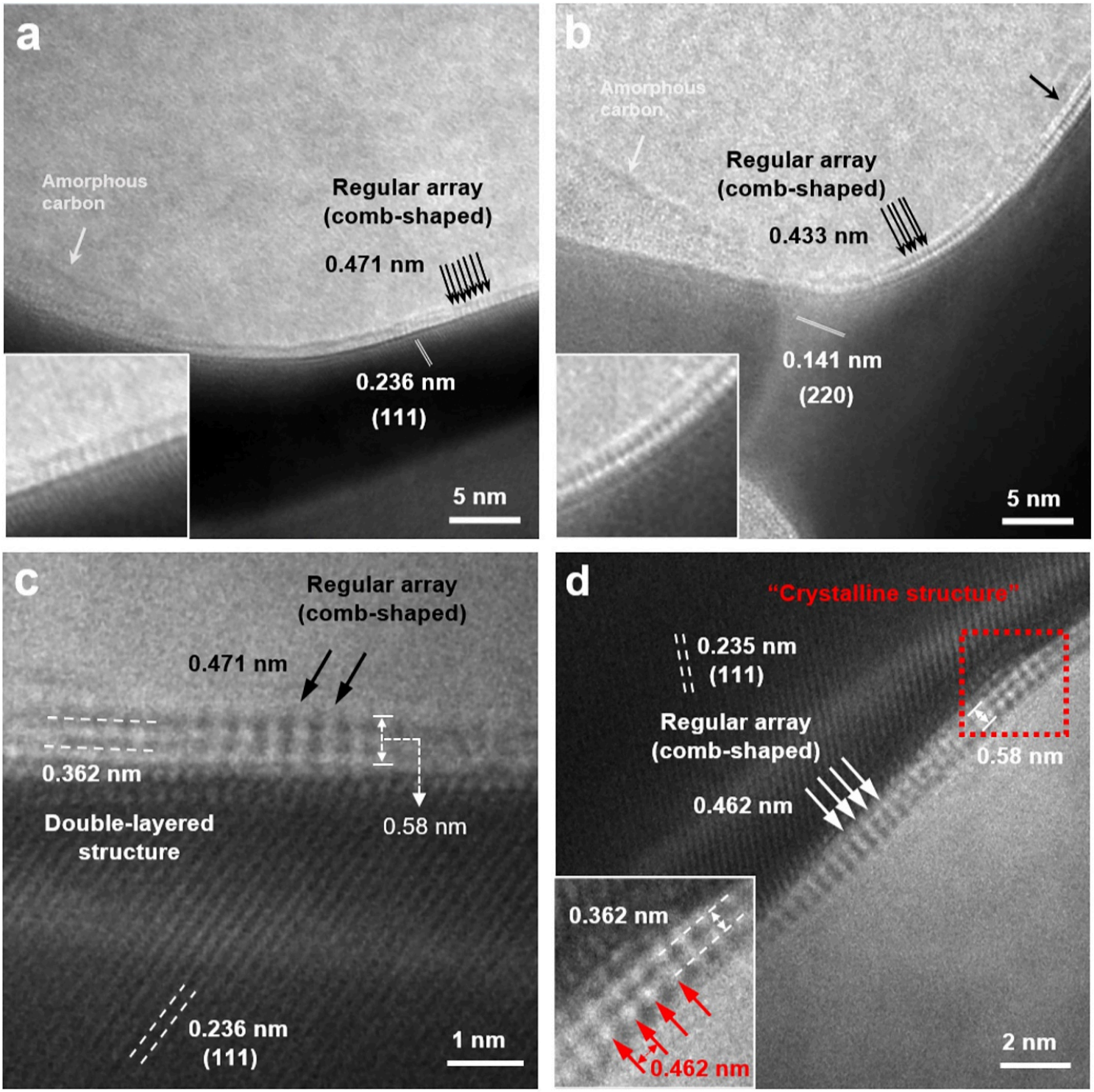


Figure 2

Varied morphologies of the adsorption structures at the early stage of CH_4 pyrolysis. a, b Comb-shaped regular arrays at the edge of Au(111) and Au(220) planes, respectively. **c,** A double-layered structure in the vicinity of a comb-shaped regular array. Both the structure heights were 0.58 nm. **d,** A "crystalline structure" with clearly identifiable atom columns. Each bright dot in the inset was designated as an atom column, as these *in situ* images were captured in transmission mode.

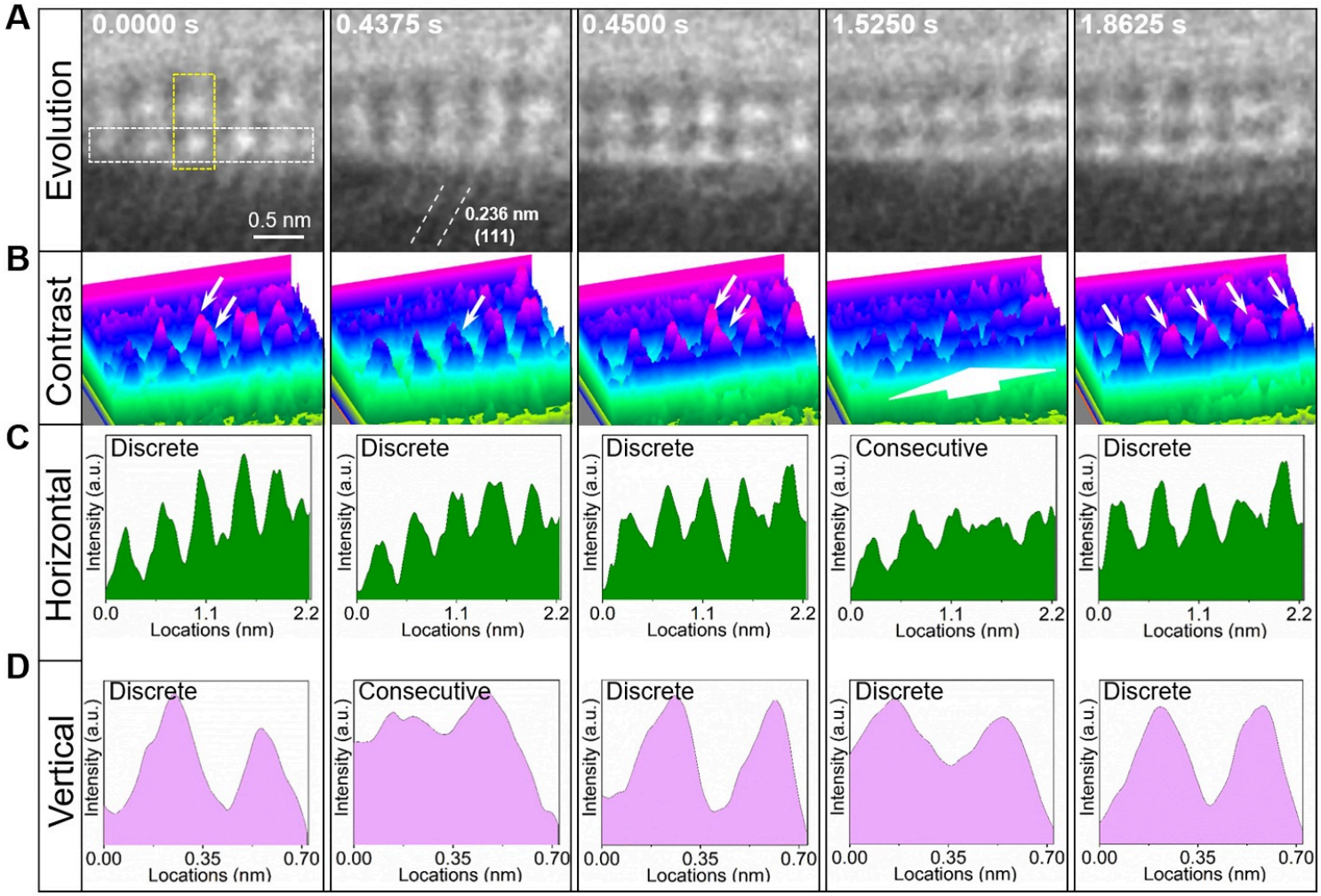


Figure 3

Evolution of the double-layered adsorption structure at the edge of Au(111) planes. a, The evolution process of a typical crystalline structure with discrete atom columns. **b,** The entire contrast analysis corresponding to the evolution images in (**a**). **c,** Contrast analysis for the horizontal atom columns during evolution indicated by white dashed boxes. **d,** Contrast analysis for the vertical atom columns during evolution indicated by yellow dashed boxes. These horizontal atom columns became almost consecutive at 1.5250 s, but restored discrete at 1.8625 s. In the vertical direction, these discrete atom columns (0.0000 s) became almost consecutive at 0.4375 s, but reversed to discrete states at 0.4500 s.

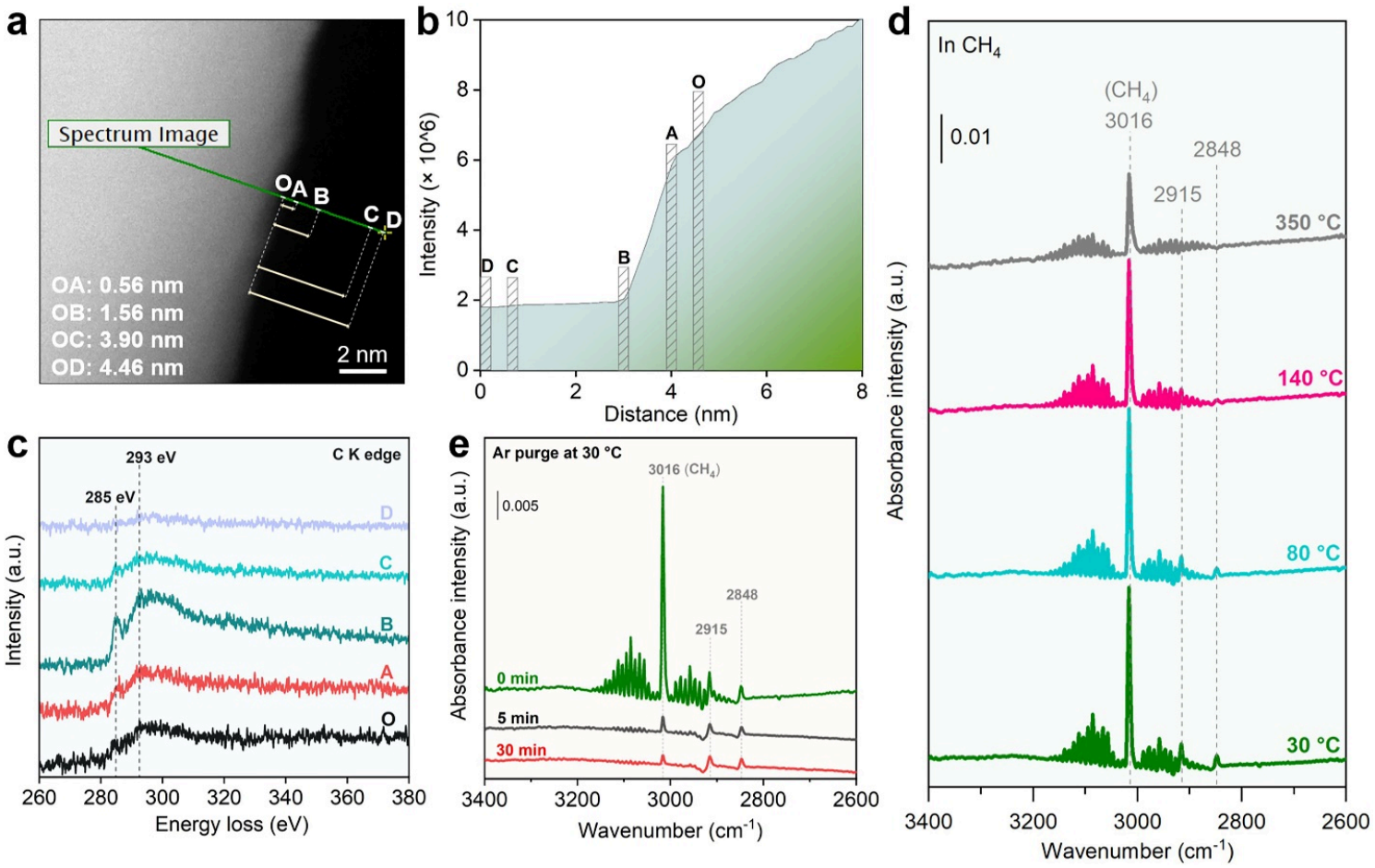


Figure 4

Composition analysis of the double-layered reaction intermediates. a, Position and distance marker for EELS line scan at different points. **b,** Contrast analysis along the green line in (**a**). **c,** EELS spectra comparison at different points in (**a**) and (**b**). **d,** The chemisorbed $-CH_2$ on the NPG surface detected by *in situ* DRIFTS under CH_4 pyrolysis conditions. The chemisorbed $-CH_2$ species (2915 and 2848 cm^{-1}) were detected when the sample chamber was cooled from 350 °C. **e,** Physisorbed CH_4 remained on the reaction-spent NPG after 30 minutes of Ar purging.

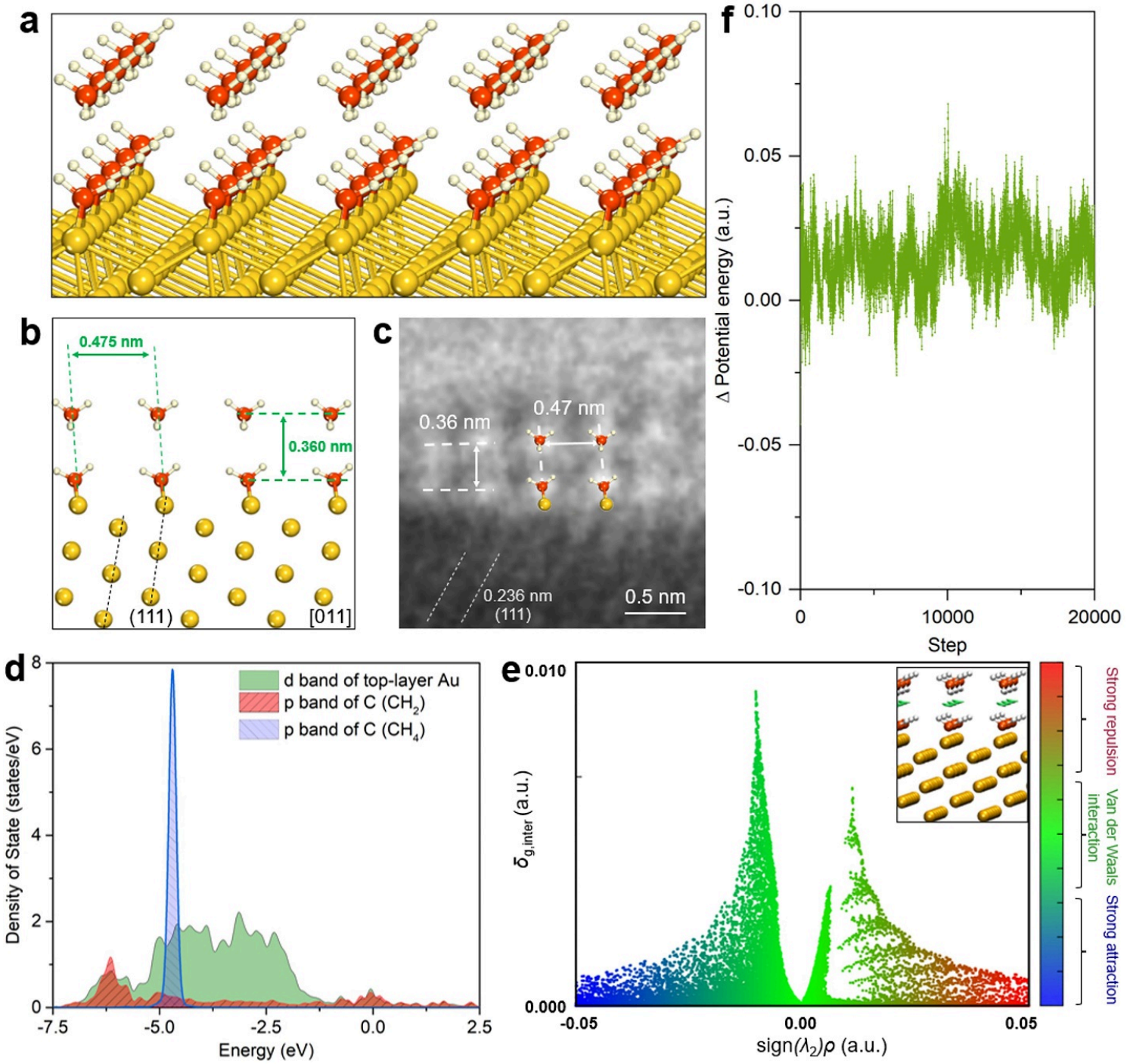


Figure 5

Theoretical analysis of the double-layered reaction intermediate adsorption structure by DFT and AIMD. **a,** The optimized stereoscopic structure for reaction intermediates adsorbing on the edge of Au(111) plane. The gold color represents Au atoms, red is for C atoms, and beige represents H atoms. **b,** The side view observed along the <011> direction of the stereoscopic structure in (**a**). The tooth spacing and interlayer distance were specified. **c,** A typical TEM image with the horizontal and vertical spacings of the adsorption structure labeled. These spacings are in good agreement with the theoretical values in (**b**). **d,** Partial density of states analysis corresponding to (**b**). **e,** The interaction analysis between $-CH_2$ and CH_4

at the edge of the Au(111) planes by an IGM method; a van der Waals interaction was identified. **f,** Potential energy during AIMD.

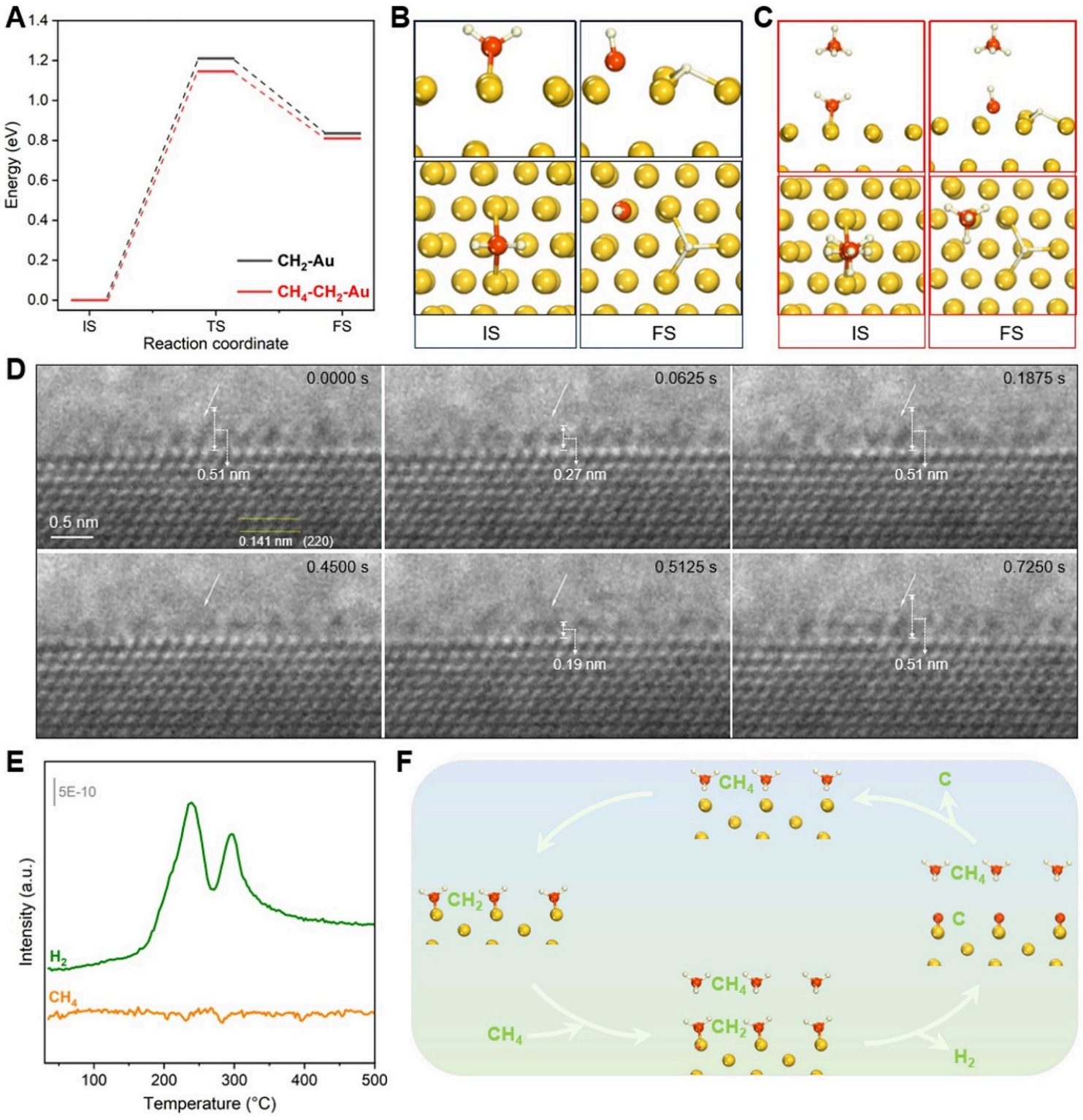


Figure 6

Reaction mechanism analysis with the double-layered reaction intermediates. a, Energy comparison of the decomposition of chemisorbed $-CH_2$ with and without CH_4 atop on the most frequently exposed Au(111) plane. The activation energy of $-CH_2$ decreases when CH_4 is physisorbed atop. The side (top)

and top (bottom) configurations of (**b**) chemisorbed $-CH_2$ without (black box) and (**c**) with (red box) CH_4 atop. IS, initial states; TS, transition states; FS, final states. The gold color represents Au atoms, red is for C atoms, and beige represents H atoms. **d,** The dynamical evolution of the double-layered reaction intermediates during CH_4 decomposition. **e,** TPD profiles of the reaction-spent NPG after 30 minutes of Ar purging. **f**, The schematic diagram of the proposed CH_4 substitution mechanism.

Supplementary Files

This is a list of supplementary files associated with this preprint. Click to download.

- NCSI0121.pdf
- SupplementaryVideo1.mp4
- SupplementaryVideo2.mp4
- SupplementaryVideo3.mp4
- SupplementaryVideo4.mp4
- SupplementaryVideo5.mp4